

Nonvolatile reconfigurable polarization rotator at datacom wavelengths based on a $\text{Sb}_2\text{Se}_3/\text{Si}$ waveguide

JORGE PARRA¹, MIROSLAVNA KOVYLINA¹, AMADEU GRIOL¹, AND PABLO SANCHIS^{1,*}

¹*Nanophotonics Technology Center, Universitat Politècnica de València, Camino de Vera s/n, 46022 Valencia, Spain*

**pabsanki@ntc.upv.es*

Abstract: Silicon photonics has become a key platform for photonic integrated circuits (PICs) due to its high refractive index and compatibility with complementary metal-oxide-semiconductor manufacturing. However, the inherent birefringence in silicon waveguides requires efficient polarization management. Here, we report a reconfigurable polarization rotator (PR) using a $\text{Sb}_2\text{Se}_3/\text{Si}$ waveguide operating at datacom wavelengths (1310 nm), providing nonvolatile switching with zero static power consumption. The polarization conversion relies on the interference of hybrid electric-magnetic (EH) modes, which can be reconfigured by changing the Sb_2Se_3 state between amorphous and crystalline. Our experimental device exhibits a polarization conversion efficiency (PCE) and a polarization extinction ratio (PER) as high as -0.08 dB and 17.65 dB, respectively, in a compact footprint of just 21 μm length. Therefore, the proposed reconfigurable PR offers a compact and energy-efficient solution for polarization management in silicon photonics, with potential applications in data communication networks and emerging applications benefiting from polarization information encodings, such as optical neural networks and quantum computing.

1. Introduction

Silicon (Si) photonics has been established during the last decade as the mainstay platform for developing photonic integrated circuits (PICs) [1]. Silicon has unique advantages, including its high refractive index contrast, which allows for the miniaturization of optical components, and its compatibility with standard complementary metal-oxide-semiconductor (CMOS) manufacturing processes, enabling cost-effective mass production. As a result, silicon PICs have been successfully developed for high-speed interconnections in data centers and a variety of sensing applications [2–4]. The prospects of silicon PICs for advancements in computing and quantum applications have also gained significant interest in recent years [5,6]. However, one of the main advantages of silicon—the high refractive index—may also give rise to a strong birefringence. This birefringence generates a polarization-dependent behavior in photonic waveguides that may hinder the design and performance of silicon devices [7]. Therefore, the control of the polarization and the possibility of implementing polarization-diversity schemes are necessary for many applications [8], making polarization rotators (PRs) vital building blocks. PR devices enable the rotation between the two orthogonal polarizations, transverse-electric (TE) and transverse-magnetic (TM), typically supported by silicon waveguides. One of the more compact solutions is based on breaking the cross-section symmetry of the waveguide, which hybridized the propagation modes, thus allowing the optical power to be periodically transferred between the TE and TM polarizations [9–11]. However, such PR devices are usually passive, hampering the reconfigurability of the polarization state. Tunable PR devices have been reported, but they are based on the power-hungry silicon thermo-optic effect [12,13].

Chalcogenide-based phase-change materials (PCMs) are currently excellent candidates for enabling reconfigurability in silicon photonic devices with ultra-low power consumption due to their unique property to switch between nonvolatile states with a large change of the refractive index [14]. Furthermore, their integration into large-scale silicon photonics platforms

has been recently demonstrated [15,16]. Among the available chalcogenides, antimony selenide (Sb_2Se_3) and antimony sulfide (Sb_2S_3) provide a change of the real part of the refractive index with negligible optical losses at telecom and datacom wavelengths [17]. Therefore, there is a strong interest in developing these materials to implement ultra-compact phase shifters with zero-static power consumption [18]. Nevertheless, such property could also be exploited to enable reconfigurability in other devices, such as mode converters [19] or microring resonators [20]. Recently, reconfigurable PRs with performance at 1550-nm optical wavelengths have been proposed through numerical simulation by adding Sb_2Se_3 in silicon photonic waveguides with breaking symmetry [21,22].

In this work, we experimentally demonstrate a reconfigurable PR in the silicon photonics platform using the ultralow-loss Sb_2Se_3 PCM in the O-band. By changing the state of the PCM, our PR can maintain the input polarization or switch to the orthogonal with a non-volatile response, i.e., zero holding power.

2. Working principle

The proposed PR consists of an asymmetric $\text{Sb}_2\text{Se}_3/\text{Si}$ waveguide. The device concept and its working principle are illustrated in **Fig. 1(a)**. Asymmetry is achieved using a narrow silicon wire and depositing a thin Sb_2Se_3 layer on top and sideways. Polarization conversion is based on the interference of two hybrid electric-magnetic (EH) modes supported by the $\text{Sb}_2\text{Se}_3/\text{Si}$ waveguide [9]. Reconfigurability is enabled by the refractive index change of the Sb_2Se_3 layer between the amorphous and crystalline states. The length of the PR is chosen to achieve an orthogonal polarization conversion between the amorphous and crystalline states. Hence, the input polarization is maintained at the device's output for the amorphous state, while polarization conversion to the orthogonal optical mode occurs at the output for the crystalline state.

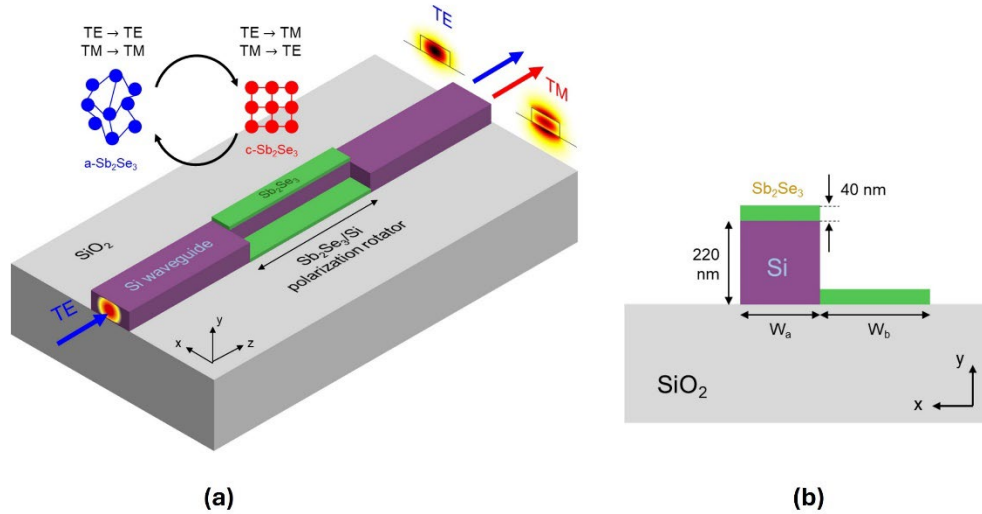


Fig. 1. Illustration of the proposed reconfigurable and nonvolatile polarization rotator based on an asymmetric $\text{Sb}_2\text{Se}_3/\text{Si}$ waveguide. **(a)** 3D view of the device and illustration of the working operation when the fundamental TE mode is launched. In the amorphous state, the polarization is maintained at the output, whereas in the crystalline state, the polarization is rotated to TM. **(b)** Cross-section of the polarization rotator. The width of the device ($W_a + W_b$) is fixed at 500 nm. The upper cladding is air.

The cross-section of the considered hybrid waveguide is shown in **Fig. 1(b)**. The design of the reconfigurable PR starts from a standard 500 nm \times 220 nm silicon-on-insulator (SOI) waveguide that is connected to a $\text{Sb}_2\text{Se}_3/\text{Si}$ waveguide with a 40-nm-thick Sb_2Se_3 layer. The

upper cladding is air. For the sake of simplicity in the device design, the width of the hybrid waveguide is set at 500 nm, and the device performance is optimized by varying the relation between the widths of the $\text{Sb}_2\text{Se}_3/\text{Si}$ wire (W_a) and Sb_2Se_3 layer placed sideways (W_b).

3. Device design and optical performance

We obtained the EH modes supported by the hybrid waveguide and their effective refractive indices, n_{eff} , as a function of the value of W_a . The optical modes were calculated using an eigenmode solver based on finite element method (FEM) (see **Appendix A.1** for simulation details). Based on the values of n_{eff} , we calculated the length required to achieve a π phase shift between the two EH modes, L_π , which gives rise to an orthogonal polarization conversion at the output. The value of L_π is given by:

$$L_\pi = \frac{\lambda}{2|n_{eff,1} - n_{eff,2}|}, \quad (1)$$

where λ is the working wavelength (1310 nm), and $n_{eff,1}$ and $n_{eff,2}$ are the effective refractive indices of the hybrid EH modes. The resulting values of L_π for the amorphous and crystalline state as a function of W_a and the L_π ratio between both states are shown in **Fig. 2(a)**. The $\text{Sb}_2\text{Se}_3/\text{Si}$ strips with a value of W_a below 200 nm give both poor optical confinement and hybridization, thus yielding ineffective interference with high insertion loss. On the other hand, as the value of W_a approximates 500 nm, the optical modes in the hybrid waveguide are less hybridized and become quasi-TE and -TM, turning off the polarization rotating performance. Consequently, based on these results, we choose $W_a = 250$ nm as the optimal value due to the high confinement and mode hybridization for both amorphous and crystalline states [**Fig. 2(b)**]. Moreover, for $W_a = 250$ nm, the ratio of L_π between the amorphous and crystalline state is a rational number. This feature allows the selection of a device length, L , exhibiting opposite interference behavior between the amorphous and crystalline state, thus providing reconfigurable polarization conversion. The normalized polarization conversion, PC , can be calculated as:

$$PC = \sin^2\left(\frac{\pi L}{2 L_\pi}\right) \quad (2)$$

and it is shown for the amorphous and crystalline state in **Fig. 2(c)**. Based on these results, polarization reconfigurability with maximum polarization conversion difference between both states is achieved for $L = 21 \mu\text{m}$.

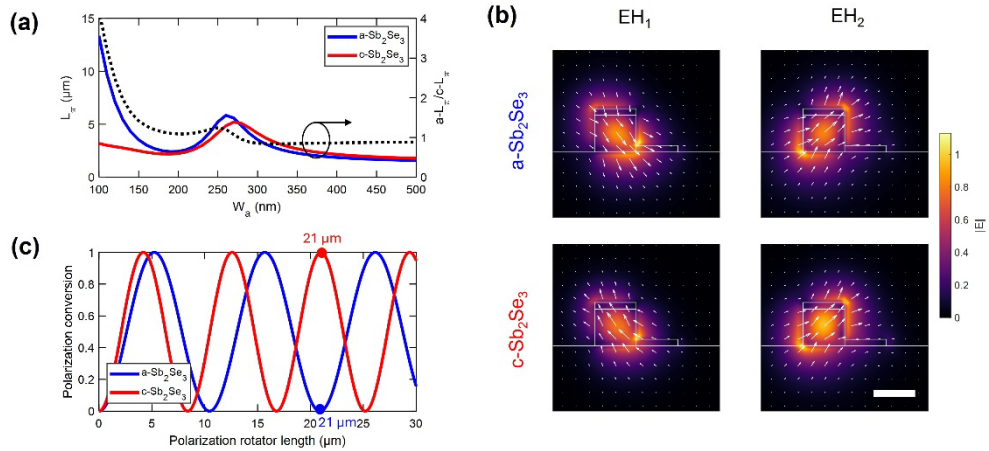


Fig. 2. (a) Length of the polarization rotator required to achieve a π phase shift between the hybrid modes, L_π , (left y-axis) as a function of the value of the W_a parameter for the amorphous

and crystalline states, and its ratio (right y-axis). **(b)** Electric field mode intensity profiles, $|E|$, and their field direction for $W_a = 250$ nm. The scale bar is 250 nm. **(c)** Normalized polarization conversion as a function of the device length for $W_a = 250$ nm and the amorphous and crystalline states. All results are given at $\lambda = 1310$ nm.

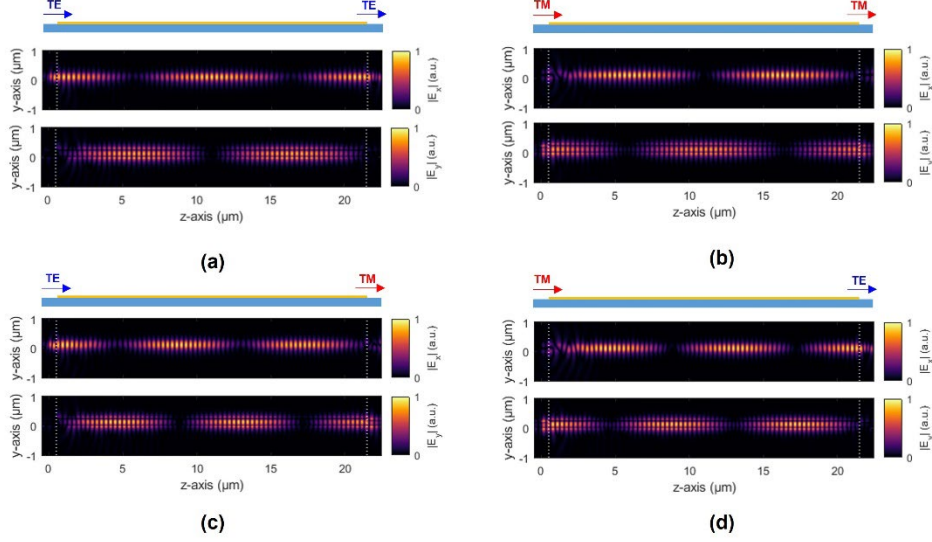


Fig. 3. $|E_x|$ and $|E_y|$ field distribution along the longitudinal cross-section of the optimal PR device for different polarization inputs and Sb_2Se_3 states. **(a)** TE launch and amorphous. **(b)** TM launch and amorphous. **(c)** TE launch and crystalline. **(d)** TM launch and crystalline. All results are given at $\lambda = 1310$ nm.

Then, we obtained the performance of the optimal PR using 3D finite-difference time-domain (3D-FDTD) simulations (Methods). **Figure 3** shows the simulated electric field distribution of the optimal 21- μm -long PR device when launching the TE and TM optical modes and for the amorphous and crystalline states. In the amorphous state [**Figs. 3(a)** and **3(b)**], we verify that the length of the PR is two times the beat length ($2L_\pi$) of the hybrid modes, thereby maintaining the polarization state at the output. On the other hand, for the crystalline state [**Fig. 3(c)** and **3(d)**], the effective optical path traveled by the hybrid EH modes is increased by L_π , thus producing a 90° rotation of the polarization at the output of the PR device.

Based on the optimal design, we analyzed the impact on the optical performance of the PR caused by variations in the thickness and refractive index of the Sb_2Se_3 layer. We carried out 3D-FDTD simulations at 1310 nm to obtain the transmission of the PR in the amorphous and crystalline states, and for the TE and TM polarization when the TE mode was launched (**Figure 4**). By considering only variations on the Sb_2Se_3 thickness, the PR keeps its reconfigurable response with a tolerance of ± 6 nm in both states although at expense of a lower polarization extinction ratio [**Figs. 4(a)** and **4(b)**]. On the other hand, by fixing the Sb_2Se_3 thickness and varying its refractive index, the PR would exhibit a more robust performance against variations in the Sb_2Se_3 refractive index [**Figs. 4(c)** and **4(d)**] compared to deviations in the thickness.

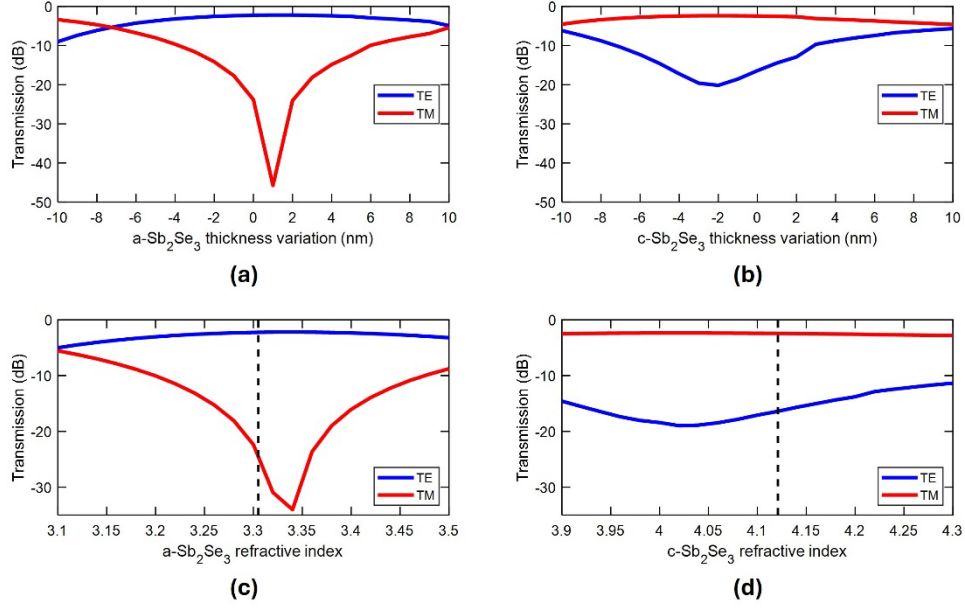


Fig. 4. Tolerance analysis of the optimal PR design against variations in the thickness and refractive index of the Sb_2Se_3 layer. Results show the transmission of the PR in the amorphous and crystalline states for the TE and TM polarization when the TE mode is launched at 1310 nm. (a,b) Sb_2Se_3 thickness variation with respect to 40 nm in the (a) amorphous and (b) crystalline states. (c,d) Sb_2Se_3 refractive index change in the (c) amorphous and (d) crystalline states. The dashed lines stand for the considered refractive index in design.

The simulated spectral performance of the optical device is shown in **Fig. 5** for the TE mode as input. A very similar performance was obtained by launching the TM mode. We calculated the polarization conversion efficiency (PCE) as:

$$PCE = \frac{P_{out}^{TE/TM}}{P_{out}^{TE} + P_{out}^{TM}} \quad (3)$$

where P_{out}^{TE} and P_{out}^{TM} is the output power contained in the TE and TM polarization, respectively, and the value of the numerator is chosen for the desired output polarization. On the other hand, the polarization extinction ratio (PER) was calculated as the ratio between the desired and undesired polarization, i.e.:

$$PER = \frac{P_{out}^{TM/TE}}{P_{out}^{TE/TM}} \quad (4)$$

Based on our simulations, near-perfect PCE [**Fig. 5(a)**], together with PER values above 20 dB [**Fig. 5(b)**], are achieved at 1310 nm. The device's insertion loss (IL) at 1310 nm is below 3 dB for both states [**Fig. 5(c)**], and it is caused by the optical mismatch between the mode profiles of the fundamental mode of the Si waveguide and the hybrid modes excited in the $\text{Sb}_2\text{Se}_3/\text{Si}$ waveguide. On the other hand, as the PR working principle is based on an interferometric effect, the bandwidth of the PR is affected by the dispersion in the effective refractive index of the hybrid modes as well as their field profile distribution, i.e., the amount of E-field in the x and y components, which also suffer wavelength dependence.

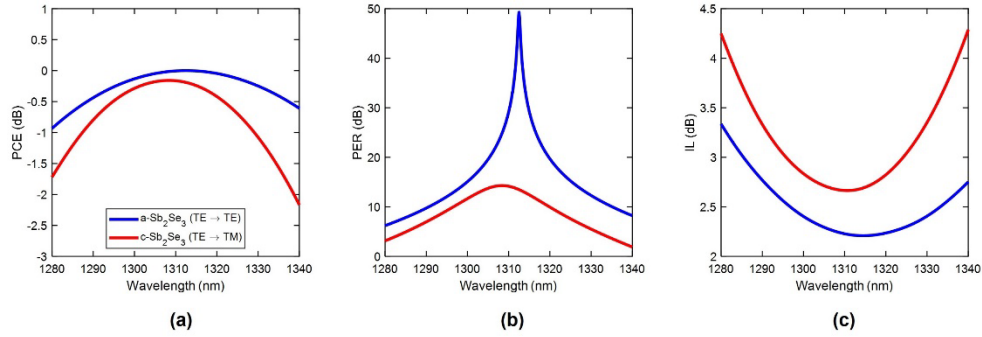


Fig. 5. Simulated spectral performance of the optimal PR device when the TE mode is launched for the amorphous (a-Sb₂Se₃) and crystalline (c-Sb₂Se₃) states. **(a)** Polarization conversion efficiency (PCE). **(b)** Polarization extinction ratio (PER). **(c)** Insertion loss (IL). Results are shown for the optimal PR and using 3D-FDTD simulations.

4. Fabrication and experimental results

We fabricated and characterized the proposed PR device on a standard 220-nm-thick SOI photonic chip (see **Appendix A.2** for fabrication details). To determine the experimental performance of the fabricated PR, we used a PIC comprised of the PR device, a polarization beam splitter (PBS), and TE- and TM-optimized grating couplers to collect separately the power contained in each polarization [**Fig. 6(a)**]. The values of W_a and W_b in the fabricated device were 280 nm and 235 nm [**Fig. 6(b)**]. Before injecting the optical power into the PR device, we polarized the light to TE using an external polarization controller and a TE reference waveguide (see **Appendix A.3** for characterization setup details). On the other hand, the PR device was first measured in the as-deposited amorphous state and then in the crystalline state by heating the chip at 250 °C for 10 min. in an Ar atmosphere.

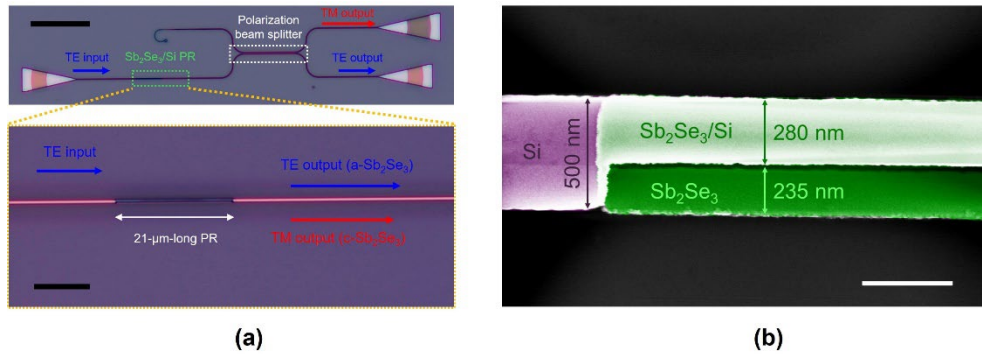


Fig. 6. (a) Optical micrograph of the PIC used to characterize the optical performance of the proposed PR device. The top and bottom scale bars are 50 μm and 10 μm , respectively. **(b)** False-color scanning electron microscope (SEM) image of the fabricated PR device. The scale bar is 400 nm.

The measured transmission of the PR under TE polarization at the input for the amorphous and crystalline states is shown in **Fig. 7**. We obtained the transmission of the PR by subtracting the spectral response of the grating couplers and PBS that were characterized from reference photonic structures as described in **Appendix B**. The experimental performance of the PR in the amorphous state shows a good agreement with the expected simulated response [**Fig. 7(a)**]. The TM output increased its optical power when the PR was switched to the crystalline state. In contrast, the TE output suffered a notable decrease caused by the polarization rotation of the optical mode at the output of the PR device [**Fig. 7(b)**]. Discrepancies between simulations and

experimental measurements could be attributed to the interplay of several factors such as variations in the actual refractive index and thickness of the Sb_2Se_3 as discussed in section 3 (see Fig. 4), as well as the slight deviation in the W_a and W_b values of the fabricated PR compared to the target values [see Fig. 6(b)].

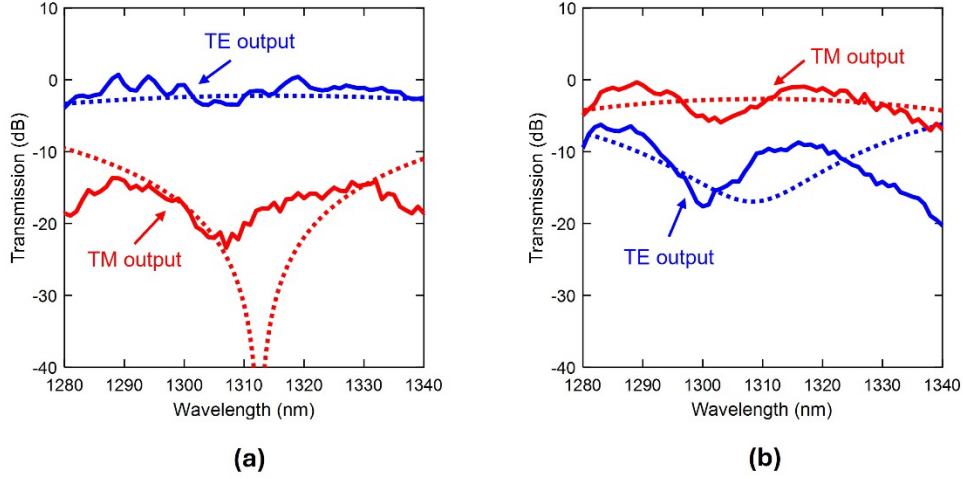


Fig. 7. Experimental (solid lines) and simulated (dotted lines) spectral response of the PR device under TE polarization at the input in the (a) amorphous and (b) crystalline states.

Based on the measured spectral response, we calculated the PCE and PER of the fabricated PR shown in Figs. 8(a) and 8(b), respectively. At 1310 nm, our PR exhibits a PCE value higher than -1 dB in both states and a PER of almost 20 dB for the amorphous state. A moderate PER of ~5 dB is found in the crystalline state.

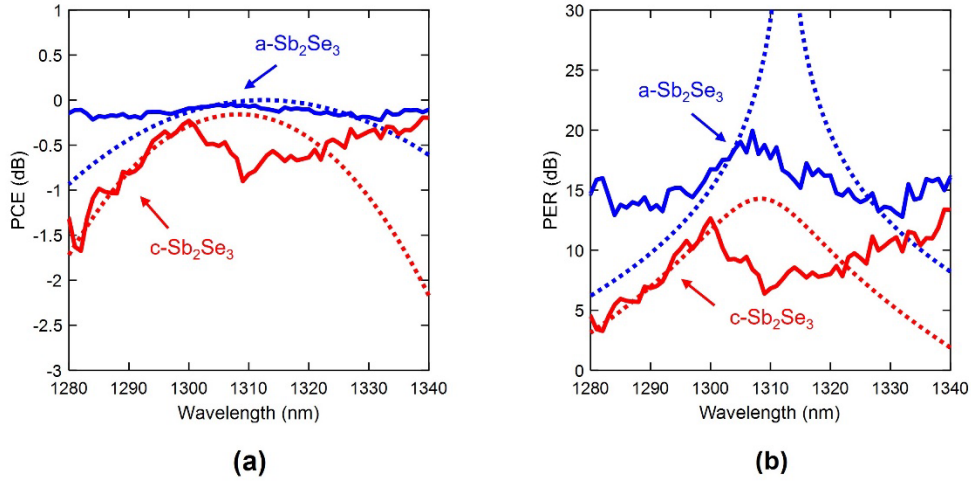


Fig. 8. Experimental (solid lines) and simulated (dotted lines) performance of the PR device in the amorphous ($a\text{-Sb}_2\text{Se}_3$) and crystalline ($c\text{-Sb}_2\text{Se}_3$) states. (a) Polarization conversion efficiency (PCE). (b) Polarization extinction ratio (PER).

5. Discussion and conclusions

In this work, we have reported a reconfigurable PR device in the SOI platform working at 1310 nm with a nonvolatile response, i.e., with zero static power consumption to hold the

reconfigurable states. Our device is based on a hybrid $\text{Sb}_2\text{Se}_3/\text{Si}$ waveguide. It can maintain the input polarization of the fundamental optical mode or switch to the orthogonal polarization by changing the Sb_2Se_3 material state between amorphous and crystalline, respectively. On the other hand, our 21- μm -long fabricated device features a PER as high as 10 dB when the polarization is rotated (Sb_2Se_3 in the crystalline state) with a low IL of 2.2 dB at 1310 nm. The IL of the device could be reduced in future work by optimizing the interface between the Si and $\text{Sb}_2\text{Se}_3/\text{Si}$ waveguide by offsetting the $\text{Sb}_2\text{Se}_3/\text{Si}$ in the x-axis to provide better overlapping and using a taper structure. According to our simulations, introducing a -100 nm displacement in the x-axis [Fig. 1(a)] would yield a reduction of the IL in both states, achieving values as low as -0.84 dB and -1 dB for the amorphous and crystalline state, respectively, at 1310 nm. On the other hand, on-chip thermo-electrical switching of our device could be implemented using transparent heaters based on graphene [23,24] or transparent conductive oxides [25–27], as well as a doped silicon-based heaters [16–18,20]. In the latter, it should be noticed that the design of the PR would rely on an asymmetric doped-Si slab waveguide to enable Joule heating. In addition, the relatively long length of the Sb_2Se_3 section may complicate the heater design due to the challenge of cooling quickly enough for an effective amorphization. In this case, a segmented approach could be considered for a more efficient dissipation of the heat [16,18].

Compared to previous silicon-based polarization management devices working at 1310 nm (**Table 1**), our PR device exhibits good optical performance compared to passive devices with a drastic improvement in terms of footprint and power consumption compared to large and power-hungry PR devices based on the silicon thermo-optic effect. The optical bandwidth could be increased by means of an adiabatic mode evolution-based rotation approach, usually achieved with asymmetric directional couplers [28], but at the expense of a larger footprint.

Table 1. Comparison of experimental silicon-based polarization control devices working in the O-band.

Ref.	Type	IL (dB)	PER (dB)	Footprint	Bandwidth	Reconfigurable	Static power consumption
[28]	PSR	<1	>15	1.6 μm \times 85 μm	80 nm	No	-
[29]	PSR	<1	>20	3 μm \times 17 μm	50 nm	No	-
[30]	PBS	<2.5	>10	28 μm \times 20 μm	80 nm	No	-
[31]	PBS	<1	>10	15 μm \times 30 μm	>100 nm	No	-
[32]	PR	<1.5	>10	300 μm \times 500 μm	60 nm	Yes (Heaters)	18 mW
This work	PR	<2.5	>5	0.5 μm \times 21 μm	40 nm	Yes (Sb_2Se_3)	Zero

PSR = Polarization splitter rotator; PBS = Polarization beam splitter; PR = Polarization rotator.

Finally, such a reconfigurable, compact, and ultralow-energy consumption PR device could serve as a key building block for photonic applications benefiting from harnessing the polarization state of light and leveraging the scalability of PICs, such as datacom networks [3], optical neural networks [33,34], or quantum computing [35,36].

APPENDIX A: METHODS

1. Optical simulations

We considered the following materials' refractive index values at 1310 nm for performing optical simulations: $n_{\text{air}} = 1$, $n_{\text{SiO}_2} = 1.444$, $n_{\text{Si}} = 3.5$, $n_{\text{a-Sb}_2\text{Se}_3} = 3.305$ (amorphous) [15], $n_{\text{c-Sb}_2\text{Se}_3} = 4.121 + j0.001$ (crystalline) [15]. We employed a FEM eigenmode solver [FemSIM tool from RSoft] to calculate the optical mode profiles and their effective refractive indices. We used a nonuniform mesh consisting of a 30 nm x 30 nm bulk grid with minimum divisions of 10 points in both the x and y axes. The simulated domain was $2 \mu\text{m} \times 2 \mu\text{m}$. The optical performance of the polarization rotator was simulated by means of 3D-FDTD using the FullWAVE tool from RSoft. In the XY plane, we used the same simulation settings as for FEM simulations. In the z-axis (propagation direction), we used a 30 nm bulk grid. A perfectly matched layer (PML) consisting of 10 PML cells was employed as the boundary condition. An overlap monitor with the TE and TM fundamental mode of the Si waveguide was placed at the device's output to determine the optical power contained in each polarization.

2. Fabrication

The integrated photonic devices were fabricated starting from a diced SOI wafer of 220 nm thick Si layer on a 3 μm thick SiO₂ buried oxide layer (SEHE). The photonic devices were patterned using an electron-beam (e-beam) lithography tool (JBX-8100FS) using an accelerating voltage of 100 kV and 500 $\mu\text{C}/\text{cm}^2$ dose. A 300 nm thick negative tone resist (ma-N 2405) was exposed for creating the silicon waveguides, whereas 270 nm and 400 nm thick positive tone resists of polymethylmethacrylate (PMMA) were utilized for defining the trenches of the grating couplers and Sb₂Se₃ windows, respectively. The silicon layer was dry-etched based on inductively coupled plasma–reactive ion etching (ICP-RIE) (Corial 210L) using a mixture of SF₆/C₄F₈ gases. The remaining resist on the photonic devices was removed using oxygen plasma for 10 min (Tepla PV200). The Sb₂Se₃ layer was fabricated by e-beam evaporation (Pfeiffer Classic 500) at a base vacuum pressure of 2.4×10^{-7} mbar and working pressure of 8×10^{-7} mbar using 4 kV High Voltage and 1.5 mA current. The rate of the deposited layer was controlled by a water-cooled quartz crystal monitor to be 0.5 $\text{\AA}/\text{s}$. A mechanical profilometer (KLA) was used to assess the final thickness of 40 ± 4 nm.

3. Optical characterization setup

The integrated photonic structures were characterized by employing an optical fiber-based setup. A continuous-wave optical signal was generated by using a stepped external-cavity tunable laser (OSICS T100). The laser output power was set to 0 dBm, and the wavelength step employed was 1 nm. The light was injected/extracted to/from the PIC grating couplers using single-mode optical fibers tilted 10° out of the plane of the chip. 3-axis motorized stages were employed for precise fiber-chip alignment. The light was polarized before being injected into the chip using a manual 3-paddle polarization controller (Thorlabs FPC032). Finally, the output light was collected using a high-sensitivity photodiode (Thorlabs S154C) connected to an optical power meter (Thorlabs PM320). All measurements were carried out at room temperature.

APPENDIX B: REFERENCE PHOTONIC STRUCTURES

We fabricated reference photonic structures comprising TE and TM grating couplers connected by 250- μm -long Si waveguides. The spectral response of these reference photonic structures is shown in **Fig. 9**. The grating period was 500 nm and 780 nm for the TE and TM grating couplers, respectively. For both designs, the fill factor was 50 %, and the etching of the trenches was 70 nm.

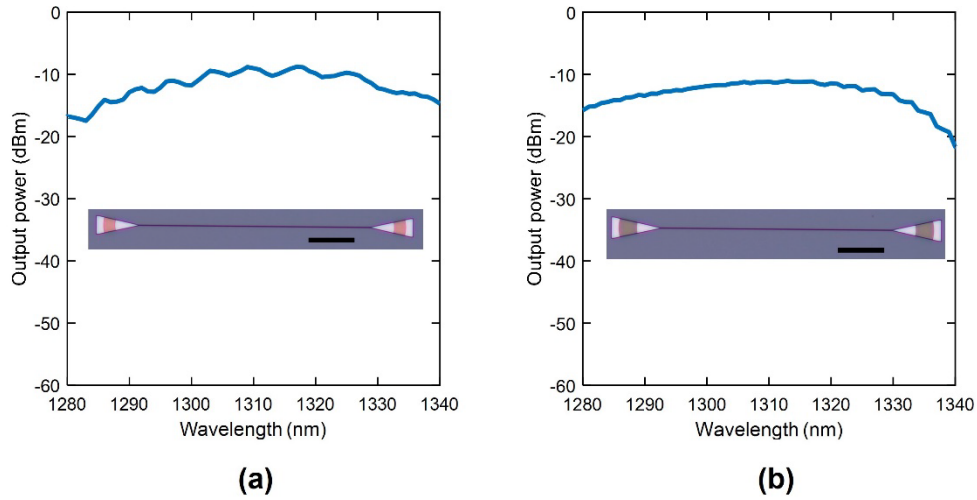


Fig. 9. Measured spectral response of reference waveguides using (a) TE- and (b) TM-designed grating couplers. The inset shows an optical micrograph of the tested reference photonic structures. The scale bar is 50 μm .

The employed PBS was based on a 41.6- μm -long symmetric directional coupler with a 300 nm gap between waveguides. The bending radius was 10 μm . The measured spectral response is shown in **Fig. 10** under a TE and TM polarized light. We measured the PBS using TE [**Fig. 10(a)**] and TM [**Fig. 10(b)**] grating couplers at both input and output.

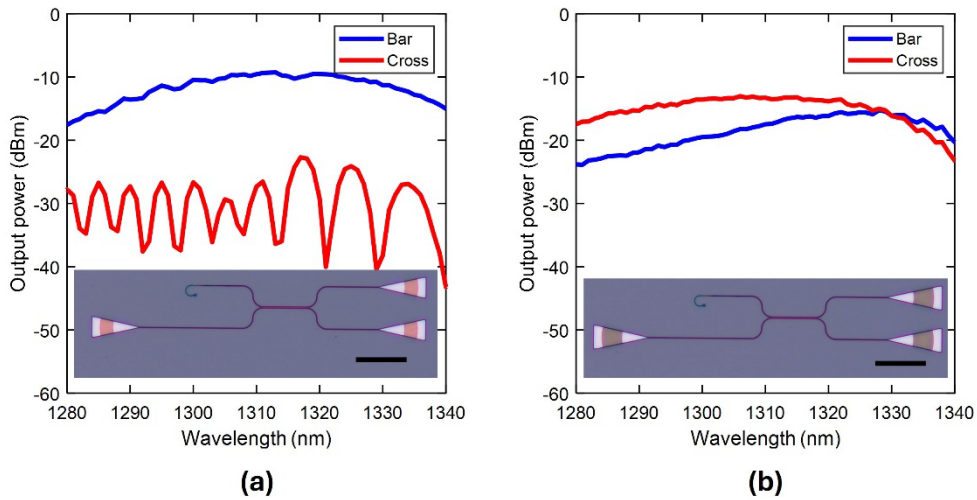


Fig. 10. Measured spectral response of the PBS structure for the (a) TE and (b) TM polarization. The top images show an optical micrograph of the measured structures. The scale bar is 50 μm .

Funding. Agencia Estatal de Investigación (TED2021-132211B-I00, PID2022-137787OB-I00); Generalitat Valenciana (PROMETEO Program (CIPROM/2022/14)); Universitat Politècnica de València (Grants PAID-06-23, PAID-10-23).

Acknowledgments. The authors would like to thank the clean room staff of the Nanophotonics Technology Center for the fabrication of the device and T. Angelova for her help with the characterization of the Sb_2Se_3 .

Disclosures. The authors declare no conflict of interest.

Data availability. Data underlying the results presented in this paper are not publicly available at this time but may be obtained from the authors upon reasonable request.

References

1. M. Lipson, "The revolution of silicon photonics," *Nat. Mater.* **21**, 974–975 (2022).
2. N. Margalit, C. Xiang, S. M. Bowers, A. Bjorlin, R. Blum, and J. E. Bowers, "Perspective on the future of silicon photonics and electronics," *Applied Physics Letters* **118**, 220501 (2021).
3. Y. Shi, Y. Zhang, Y. Wan, Y. Yu, Y. Zhang, X. Hu, X. Xiao, H. Xu, L. Zhang, and B. Pan, "Silicon photonics for high-capacity data communications," *Photon. Res.* **10**, A106 (2022).
4. S. Shekhar, W. Bogaerts, L. Chrostowski, J. E. Bowers, M. Hochberg, R. Soref, and B. J. Shastri, "Roadmapping the next generation of silicon photonics," *Nat Commun* **15**, 751 (2024).
5. B. J. Shastri, A. N. Tait, T. Ferreira De Lima, W. H. P. Pernice, H. Bhaskaran, C. D. Wright, and P. R. Prucnal, "Photonics for artificial intelligence and neuromorphic computing," *Nat. Photonics* **15**, 102–114 (2021).
6. J. Bao, Z. Fu, T. Pramanik, J. Mao, Y. Chi, Y. Cao, C. Zhai, Y. Mao, T. Dai, X. Chen, X. Jia, L. Zhao, Y. Zheng, B. Tang, Z. Li, J. Luo, W. Wang, Y. Yang, Y. Peng, D. Liu, D. Dai, Q. He, A. L. Muthali, L. K. Oxenløwe, C. Vighiar, S. Paesani, H. Hou, R. Santagati, J. W. Silverstone, A. Laing, M. G. Thompson, J. L. O'Brien, Y. Ding, Q. Gong, and J. Wang, "Very-large-scale integrated quantum graph photonics," *Nat. Photon.* **17**, 573–581 (2023).
7. D. Dai, L. Liu, S. Gao, D. Xu, and S. He, "Polarization management for silicon photonic integrated circuits," *Laser & Photonics Reviews* **7**, 303–328 (2013).
8. T. Barwicz, M. R. Watts, M. A. Popović, P. T. Rakich, L. Soccia, F. X. Kärtner, E. P. Ippen, and H. I. Smith, "Polarization-transparent microphotonic devices in the strong confinement limit," *Nature Photon* **1**, 57–60 (2007).
9. M. Aamer, A. M. Gutierrez, A. Brimont, D. Vermeulen, G. Roelkens, J.-M. Fedeli, A. Hakansson, and P. Sanchis, "CMOS Compatible Silicon-on-Insulator Polarization Rotator Based on Symmetry Breaking of the Waveguide Cross Section," *IEEE Photon. Technol. Lett.* **24**, 2031–2034 (2012).
10. L. Jia, T.-Y. Liow, J. Song, X. Luo, N. Duan, S. C. Koh, Q. Fang, M. Yu, and G. Lo, "Compact Optical Polarization Rotators Based on an Asymmetric Silicon Waveguide," *IEEE Photon. Technol. Lett.* **25**, 2229–2232 (2013).
11. A. Xie, L. Zhou, J. Chen, and X. Li, "Efficient silicon polarization rotator based on mode-hybridization in a double-stair waveguide," *Opt. Express* **23**, 3960 (2015).
12. J. D. Sarmiento-Merenguel, R. Halir, X. L. Roux, C. Alonso-Ramos, L. Vivien, P. Cheben, E. Durán-Valdeiglesias, I. Molina-Fernández, D. Marris-Morini, D.-X. Xu, J. H. Schmid, S. Janz, and A. Ortega-Moñux, "Demonstration of integrated polarization control with a 40 dB range in extinction ratio," *Optica* **2**, 1019–1023 (2015).
13. Q. Xu, L. Chen, M. G. Wood, P. Sun, and R. M. Reano, "Electrically tunable optical polarization rotation on a silicon chip using Berry's phase," *Nat Commun* **5**, 5337 (2014).
14. R. Chen, Z. Fang, F. Miller, H. Rarick, J. E. Fröch, and A. Majumdar, "Opportunities and Challenges for Large-Scale Phase-Change Material Integrated Electro-Photonics," *ACS Photonics* **9**, 3181–3195 (2022).
15. M. Delaney, I. Zeimpekis, D. Lawson, D. W. Hewak, and O. L. Muskens, "A New Family of Ultralow Loss Reversible Phase-Change Materials for Photonic Integrated Circuits: Sb₂S₃ and Sb₂Se₃," *Adv Funct Materials* **30**, 2002447 (2020).
16. R. Chen, V. Tara, M. Choi, J. Dutta, J. Sim, J. Ye, Z. Fang, J. Zheng, and A. Majumdar, "Deterministic quasi-continuous tuning of phase-change material integrated on a high-volume 300-mm silicon photonics platform," *npj Nanophoton.* **1**, 7 (2024).
17. M. Wei, K. Xu, B. Tang, J. Li, Y. Yun, P. Zhang, Y. Wu, K. Bao, K. Lei, Z. Chen, H. Ma, C. Sun, R. Liu, M. Li, L. Li, and H. Lin, "Monolithic back-end-of-line integration of phase change materials into foundry-manufactured silicon photonics," *Nat Commun* **15**, 2786 (2024).
18. C. Rios, Q. Du, Y. Zhang, C.-C. Popescu, M. Y. Shalaginov, P. Miller, C. Roberts, M. Kang, K. A. Richardson, T. Gu, S. A. Vitale, and J. Hu, "Ultra-compact nonvolatile phase shifter based on electrically reprogrammable transparent phase change materials," *Photonix* **3**, 26 (2022).
19. X. Luo, H. Ye, M. Zhou, S. Zhang, Y. Sun, X. Wang, J. Li, L. Chen, and Y. Liu, "Inverse design of deformed Sb₂Se₃ stripes in silicon waveguide for reconfigurable mode converters," *Opt. Mater. Express* **13**, 2834 (2023).
20. Z. Fang, B. Mills, R. Chen, J. Zhang, P. Xu, J. Hu, and A. Majumdar, "Arbitrary Programming of Racetrack Resonators Using Low-Loss Phase-Change Material Sb₂Se₃," *Nano Lett.* **24**, 97–103 (2024).
21. H. Jin, L. Niu, J. Zheng, P. Xu, and A. Majumdar, "Compact nonvolatile polarization switch using an asymmetric Sb₂Se₃-loaded silicon waveguide," *Opt. Express* **31**, 10684 (2023).
22. J. Parra, J. Navarro-Arenas, and P. Sanchis, "Sb₂Se₃/Si tunable rotator with ultra-compact footprint," in *2023 IEEE Silicon Photonics Conference (SiPhotonics)* (IEEE, 2023), pp. 1–2.
23. Z. Fang, R. Chen, J. Zheng, A. I. Khan, K. M. Neilson, S. J. Geiger, D. M. Callahan, M. G. Moebius, A. Saxena, M. E. Chen, C. Rios, J. Hu, E. Pop, and A. Majumdar, "Ultra-low-energy programmable non-volatile silicon photonics based on phase-change materials with graphene heaters," *Nat. Nanotechnol.* **17**, 842–848 (2022).

24. J. Faneca, S. Meyer, F. Y. Gardes, and D. N. Chigrin, "Graphene microheater for phase change chalcogenides based integrated photonic components [Invited]," *Opt. Mater. Express* **12**, 1991 (2022).
25. H. Taghinejad, S. Abdollahramezani, A. A. Eftekhar, T. Fan, A. H. Hosseinnia, O. Hemmatyar, A. Eshaghian Dorche, A. Gallmon, and A. Adibi, "ITO-based microheaters for reversible multi-stage switching of phase-change materials: towards miniaturized beyond-binary reconfigurable integrated photonics," *Opt. Express* **29**, 20449 (2021).
26. J. Parra, J. Hurtado, A. Griol, and P. Sanchis, "Ultra-low loss hybrid ITO/Si thermo-optic phase shifter with optimized power consumption," *Opt. Express* **28**, 9393 (2020).
27. W. Tong, E. Yang, Y. Pang, H. Yang, X. Qian, R. Yang, B. Hu, J. Dong, and X. Zhang, "An Efficient, Fast-Responding, Low-Loss Thermo-Optic Phase Shifter Based on a Hydrogen-Doped Indium Oxide Microheater," *Laser & Photonics Reviews* 2201032 (2023).
28. Y.-J. Hung, C.-H. Chen, H.-C. Chung, J.-Z. Lai, and S.-Y. Tseng, "Compact and broadband silicon polarization splitter-rotator using adiabaticity engineering," *Opt. Lett.*, OL **49**, 1852–1855 (2024).
29. X. Ruan, H. Li, and T. Chu, "Inverse-Designed Ultra-Compact Polarization Splitter-Rotator in Standard Silicon Photonic Platforms With Large Fabrication Tolerance," *J. Lightwave Technol.* **40**, 7142–7149 (2022).
30. N. Zhao, C. Qiu, Y. He, Y. Zhang, and Y. Su, "Broadband Polarization Beam Splitter by Using Cascaded Tapered Bent Directional Couplers," *IEEE Photonics J.* **11**, 1–8 (2019).
31. S. Mao, L. Cheng, C. Zhao, and H. Y. Fu, "Ultra-broadband and ultra-compact polarization beam splitter based on a tapered subwavelength-grating waveguide and slot waveguide," *Opt. Express* **29**, 28066 (2021).
32. Y. Bai, P. Wang, B. Peng, and T. Chu, "O-band reconfigurable silicon polarization rotator," *Chin. Opt. Lett.* **22**, 011303 (2024).
33. J. Li, Y.-C. Hung, O. Kulce, D. Mengu, and A. Ozcan, "Polarization multiplexed diffractive computing: all-optical implementation of a group of linear transformations through a polarization-encoded diffractive network," *Light Sci Appl* **11**, 153 (2022).
34. K. Liao, T. Dai, Q. Yan, X. Hu, and Q. Gong, "Integrated Photonic Neural Networks: Opportunities and Challenges," *ACS Photonics* **10**, 2001–2010 (2023).
35. J. Wang, F. Sciarrino, A. Laing, and M. G. Thompson, "Integrated photonic quantum technologies," *Nat. Photonics* **14**, 273–284 (2020).
36. W. Luo, L. Cao, Y. Shi, L. Wan, H. Zhang, S. Li, G. Chen, Y. Li, S. Li, Y. Wang, S. Sun, M. F. Karim, H. Cai, L. C. Kwek, and A. Q. Liu, "Recent progress in quantum photonic chips for quantum communication and internet," *Light Sci Appl* **12**, 175 (2023).